Accurate Internal Monitoring of Batteries by Embedded Piezoelectric Sensors

Ezzoubair Bendadesse, Pierre Lemaire, Pascal Travers, Jean-Marie Tarascon, Ozlem Sel

Accurate Internal Monitoring of Batteries by Embedded Piezoelectric Sensors

Ezzoubair Bendadesse[a,b,c], Pierre Lemaire [a,c], Pascal Travers,[a]

Jean-Marie Tarascon[a,c]* and Ozlem Sel[a,c]*

[a] *Chimie du Solide et de l'Energie, UMR 8260, Collège de France, 75231 Paris, Cedex 05, France*

[b] *Sorbonne Université, CNRS, Laboratoire Interfaces et Systèmes Electrochimiques, LISE, UMR 8235, 75005 Paris, France*

[c] *Réseau sur le Stockage Electrochimique de l'Energie (RS2E), CNRS FR 3459, 80039 Amiens Cedex, France*

Corresponding authors:

jean.marie-tarascon@college-de-france.fr

ozlem.sel@college-de-france.fr

Keywords: EQCM, piezoelectric sensors, electrode/electrolyte interface, Lithium ion battery, Sodium ion battery

Abstract

Advancements in operando techniques have unraveled the complexities of the Electrode Electrolyte Interface (EEI) in electrochemical energy storage devices. However, each technique has inherent limitations, often necessitating adjustments to experimental conditions, which may compromise accuracy. To address this challenge, a novel battery cell design was introduced, integrating piezoelectric sensors with electrochemical analysis for surface-sensitive operando measurements. This innovative approach aims to overcome conventional limitations by accommodating commercial-grade battery electrodes within a single body, alongside a piezoelectric sensor. This enables operando electrogravimetric measurements to be realized, and the electrochemistry of a battery to be more faithfully reproduced at the sensor level. A proof of concept was carried out on both Li-ion ($LiFePO_4$//Graphite) and Na-ion ($Na_3V_2(PO_4)_2F_3$//Hard carbon) systems, utilizing commercially available powder electrodes. In both cases, the results revealed rational mass variations at the sensor level during the cycling of commercial electrodes with mass loadings several orders of magnitude higher, while performing Galvanostatic Charge Discharge (GCD) tests across various C-rates. This innovative design opens up possibilities for a broader application of operando electrogravimetry within the battery community, to enhance our understanding of EEI behavior and facilitate the development of more efficient energy storage solutions.

1. Introduction

As the global need for energy storage is rapidly growing, researchers are exploring new strategies to elevate batteries to a higher level of performance in terms of both capacity and durability, while enhancing their safety.[1] The focus has been on not only discovering new materials but also developing a wide array of sophisticated diagnostic techniques. This enables the prediction of cathode or anode electrodes' behavior in the presence of electrolytes during cycling and the examination of processes leading to the evolution of their interfaces. They are crucial for advancing electrochemical energy storage devices (batteries or supercapacitors), and remain a true challenge in electrochemistry.

One strategy to overcome this challenge involves implementing sensing technologies (optical,[2] acoustic,[3] *etc.*) that allow for the real-time monitoring of interface processes occurring within a battery. In this regard, there has been increasing interest in piezoelectric sensors used in conjunction with electrochemical analysis, namely the Electrochemical Quartz Crystal Microbalance (EQCM) and its derived methods.[4], [5], [6], [7]

In line with this progress, EQCM cells have undergone significant advancements to enable its use with other methods, such as EIS[8], or to operate under conditions that closely simulate those encountered in battery applications. Levi *et al.* made significant advancements in the field by introducing hermetic multiharmonic EQCM with dissipation monitoring (EQCM-D) cell and employing them for the first time with air-sensitive organic electrolytes and alkali metals.[6a, 9] Similar to earlier studies, a design described by Kitz *et al.* is also a modification of a commercial EQCM-D cell, which provides the opportunity to combine EQCM-D and EIS measurements.[6b, 8, 10] Our group has also contributed to this evolution by developing universal hermetically sealed cells adapted to most commercial EQCM devices and served to study several battery chemistry. [5, 7b], [11], [12]

Thus far, a common aspect of the non-aqueous electrolyte/electrode interface research surveyed is their execution in a half-cell configuration (e.g. metallic Li as a counter electrode) or solely employing voltage-controlling techniques (CV or linear sweep voltammetry (LSV)).[6, 13] These methods have proven to be effective in elucidating the behavior of the targeted system, such as the electrochemical stability window of the electrolyte, the disentanglement of faradaic and capacitive contributions, and the impact of the scan rate on redox process polarization. However, to evaluate

the performance of battery systems under diverse cut-off voltages and current densities, it is imperative to use Galvanostatic Charge Discharge (GCD) techniques. This will enable a direct correlation between EQCM measurements and the phenomena observed in charge-discharge profiles further mimicking real-life battery assessment. However, the utilization of current-controlling electrochemical techniques, such as GCD, poses challenges when working with quartz resonators due to the minute loadings (few micrograms) involved. To cycle such small quantities of active material requires currents in the range of nanoamperes, particularly for slow C-rates such as C/10 or C/20. Thus, parasitic currents arising from electrical components can overwhelm the imposed current leading to experiment failure. Kitz's approach,[6b] which involves connecting the small-loading QCM to a larger loading electrode (sprayed on a mesh), may address the issue of ultra-low current. However, the use of a sprayed electrode introduces challenges related to capacity balancing and current estimation.[14] Therefore, a sensor incorporated directly at the cell level is more relevant to provide information inside from a functioning battery.

To circumvent such technical problems and to provide a closer picture of what happens in real-life batteries, device development is necessary. Herein, we describe the design and development of an improved version of the EQCM testing apparatus that allows accurate electrogravimetric measurements under full-cell conditions, with the idea of placing a piezoelectric QCM sensor in an "over-sized coin cell". Two types of powder electrodes pertaining to commercial Li-ion and Na-ion systems (Lithium iron phosphate (LFP)//Graphite (Gr) and Sodium vanadium fluorophosphates (NVPF)//Hard carbon (HC)) were probed for proof-of-concept.

2. Experimental Section

2.1 Electrode preparation: Lithium iron phosphate (LFP) powder from Umicore (Belgium) was used as the active material along with carbon super P (Csp) (conductive additive) and Poly(vinylidene fluoride-co-hexafluoropropylene) (PVDF-HFP) (binder). A slurry composed of LFP:Csp:PVDF-HFP (72:18:10 in *wt.*) was prepared using N-methyl-2-pyrrolidone (NMP) as the solvent. The slurry was sprayed onto the Platinum electrode of a quartz resonator (AT-cut 9MHz from Bio-Logic, France), leading to LFP coated QCM electrode. LFP and graphite electrodes with a loading of 13 mg cm^{-2} and 8 mg cm^{-2}, respectively, were used as received from Li-FUN

technology (China). LP30 electrolyte (1M $LiPF_6$ in ethylene carbonate and dimethyl carbonate (EC/DMC) 1:1 wt.) (Elyte) was used for all LFP//Graphite QCM embedded battery cell tests.

$Na_3V_2(PO_4)_2F_3$ (Sodium vanadium fluorophosphate (NVPF)) and Hard carbon (HC) powders were obtained from Tiamat Energy (France). NVPF slurry had the same recipe as LFP, as described above. HC containing slurry was composed of 94% *wt.* of active materials and 6% *wt.* PVDF-HFP. Respective slurry was sprayed onto Platinum electrode of a quartz resonator, leading to NVPF and HC coated QCM electrodes. NVPF and HC electrodes with a loading of 10 mg cm^{-2} and 4.5 mg cm^{-2}, respectively, were used as received from the same company. 1M $NaPF_6$ in EC:PC:DMC (ethylene carbonate:propylene carbonate:dimethyl carbonate, 1:1:1 in volume) was used as an electrolyte for all NVPF//HC QCM embedded battery cell tests.

The loading on all the quartz was kept between 15-50 µg cm^{-2} (estimated by the resonant frequency difference of the bare and the loaded QCM), a lower loading was used for NVPF and HC electrodes to ensure good signal quality and the validity of the Sauerbrey regime.[15]

2.2 QCM sensor embedded battery cell design: The foundation of the new design is based on our former EQCM cell (**Figure 1a**), which has been documented in a patent application filed in 2020.[16] **Figure 1b** showcases the modifications implemented on the original cell design. The upper portion of the cell has been replaced, and three distinct parts have been introduced to accommodate battery components in a manner reminiscent of an "oversized" coin cell. This modification creates two separate compartments that are interconnected by a cylindrical cavity designed to contain the electrolyte. To ensure optimal and uninterrupted flow of alkali ions, a stainless-steel mesh is placed as shown in **Figure 1b**, followed by the investigated electrode, mimicking the assembly of a coin-cell. Separators, a counter electrode, a spacer and a spring are then added to complete the battery structure.

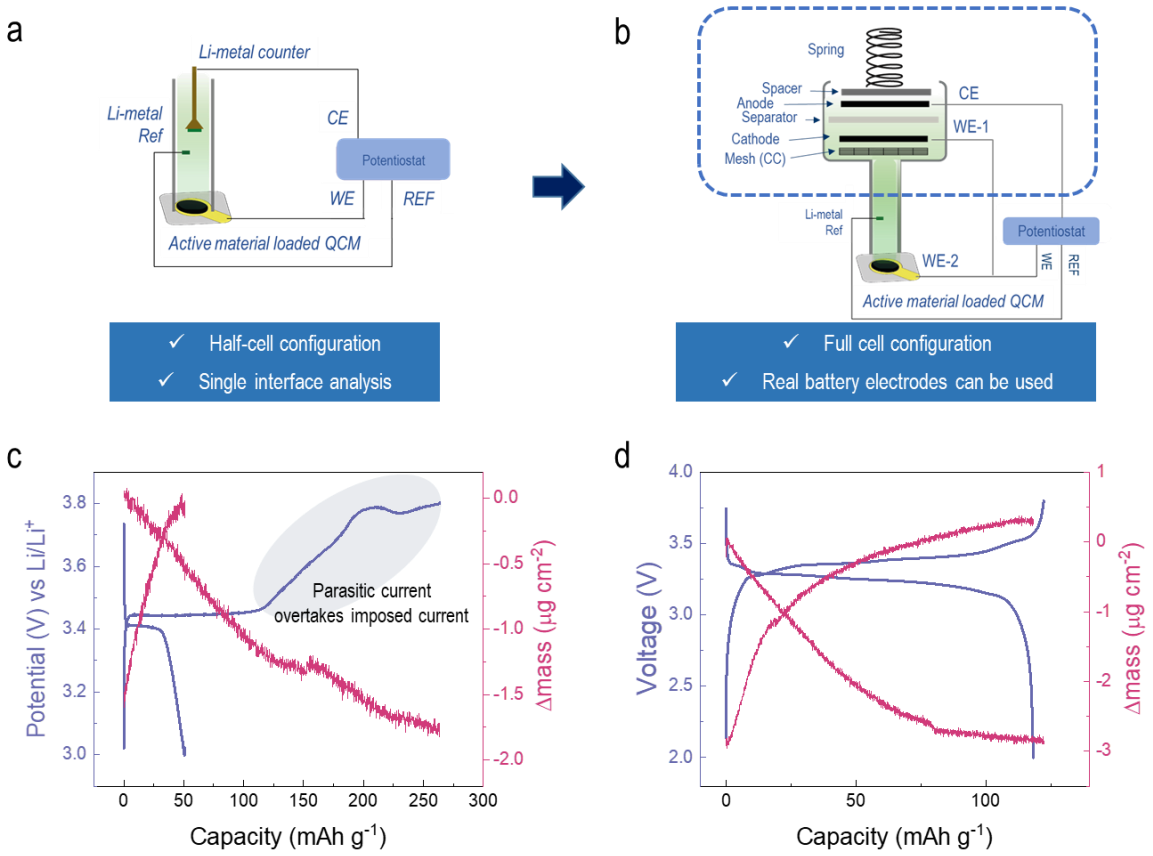

Figure 1. QCM as a piezoelectric sensor for probing battery interfaces versus half-cell configuration. **a)** Scheme of the former half-cell design and **b)** new design where WE-1 and WE-2 are the real working and loaded quartz resonator (cathode electrode in this representation), CE is the counter electrode (anode in this representation). WE-2 can be loaded either with the anode composite electrode or cathode composite electrode. **c)** Charge/discharge profile of LFP-coated QCM resonator using the half-cell EQCM test apparatus and **d)** LFP//Graphite battery cell, mass response is measured on the LFP-coated QCM sensor. The rate used for the GCD test is C/5 on a ~25 μg cm^{-2} loaded quartz. 2nd cycle is shown.

Figure 1b also depicts a schematic representation of the cell and the external circuitry, wherein the quartz resonator is deliberately short-circuited to the real working electrode. This intentional short-circuiting ensures an accurate replication of the electrochemical behavior at the quartz level, effectively extending the functionality of the active material coated onto the quartz to serve as an adjunct to the actual working electrode. Consequently, the utilization of lower C-rates in GCD tests becomes viable, devoid of any disruptive parasitic currents that might perturb the measurements.

Further details of the cell assembly, operation and validation steps are given in Supporting Information.

2.3 Electrochemical/gravimetric tests: The resonators modified with the $LiFePO_4$ (LFP), $Na_3V_2(PO_4)_2F_3$ (NVPF) or HC thin films together with the commercial cathode and anode electrodes were mounted in the battery test apparatus developed in the present work (**Figure 1b**). The cell is mounted in an Ar-filled glove-box and the measurements were conducted outside the glove-box. The EQCM with motional resistance monitoring (EQCM-R) was performed using a Biologic SP200 workstation coupled with a commercial SEIKO QCM922A microbalance which permitted the resonance frequency (f) along with the motional resistance (R_m) to be monitored during electrochemical cycling. Coated QCMs were short-circuited with the corresponding commercial electrode, so that they acted as an extension of the latter (e.g., LFP coated QCM with LFP (Li-FUN)). The cell was cycled using galvanostatic cycling with potential limitation (GCPL) (C-rates indicated on the figures) and the frequency response (f) and the motional resistance (R_m) of the coated QCM resonator was simultaneously monitored.

3. Results and Discussion

As user requirements for a better representation of real battery operating conditions evolve, we recognize limitations in previous EQCM cell designs. Their drawback is mainly rooted in the minimal mass loading on QCM sensors, which limits the use of low currents associated with small C-rates. Indeed, the loading on these quartz electrodes must not exceed ~50 µg cm^{-2} to ensure high-quality frequency signal and reliable interpretations. Consequently, slow C-rate tests (C/10 or C/20) require nanoampere-level currents vulnerable to parasitic currents, inevitably leading to experiment failure. This feature is exemplified in the charge/discharge profile of $LiFePO_4$-coated QCM resonator (**Figure 1c**) using our former half-cell EQCM test apparatus (**Figure 1a**). Moreover, the lack of real composite electrodes representative of the materials used in practical battery systems prevents more accurate characterization of real-world battery performance. Our new design (**Figure 1b**, see **Experimental Part 2.2**) incorporates solutions to above-mentioned concerns. As a first test, we studied the LFP interface using the new cell design and compared with that obtained in **Figure 1c.** In these tests, WE-1 and WE-2 (**Figure 1b**) are the real working (LFP

commercial electrode (Li-FUN, China)) and LFP-loaded quartz resonator, respectively; whereas the CE is the commercial graphite electrode. **Figure 1d** illustrates the charge/discharge profile along with the concurrently observed mass response on a QCM sensor coated with LFP, integrated into an LFP//Graphite cell, which was not possible with the previous design (**Figure 1c**).

In the following section, we will use this new cell design to observe (electro)chemical and gravimetric phenomena in two separate cells as proof-of-concept, starting with the LFP//Gr and progressing to the NVPF//HC chemistry.

3.1 Monitoring electrochemical and gravimetric events in powder electrodes from commercial Li- and Na-ion cells

3.1.1 $LiFePO_4$ // Graphite cell

The iron phosphate/graphite pairing represents one of the most extensively commercialized Li-ion technologies thanks to its safety and environmental advantages while offering an attractive energy density (210 Wh/kg). However, some issues remain regarding the influence of different parameters, such as C-rate and upper potential cutoff, on the longevity of iron phosphate batteries. Among the numerous observed degradation mechanisms in LFP//Gr batteries, several are associated with mass variation at the electrode level, such as lithium plating and solid-electrolyte interface (SEI) thickening,[17] as well as iron dissolution at high temperatures together with the loss of active Li ions.[18] This was an impetus to use QCM sensor as a mean to assess mass variation at the interface level, aiming at quantifying the magnitude of each degradation.

Figure 2 depicts the charge/discharge cycling of the LFP//Gr system, performed at a C/5 rate in LP30, where LFP coated QCM sensor is short-circuited with the commercial LFP cathode. **Figure 2a** present the simultaneously obtained QCM sensor's mass (Δm) and the motional resistance change (ΔR_m) over cycling about 60 h. Small $\Delta R_m/\Delta f$ ratio (which can also be presented as $|\Delta W| << |\Delta f/|$, where W is the full width of the resonance peak at half height, **Figure S4**) permitted the direct translation of the frequency signal to mass changes. Notably, during the charging process (delithiation), a reduction in mass is observed, while during discharge (lithiation), an increase in mass is detected. This observation validates that the electrochemical behavior of the LFP coating on the quartz electrode aligns with that of the larger LFP electrode, to which it is electrically connected via a short-circuit arrangement.

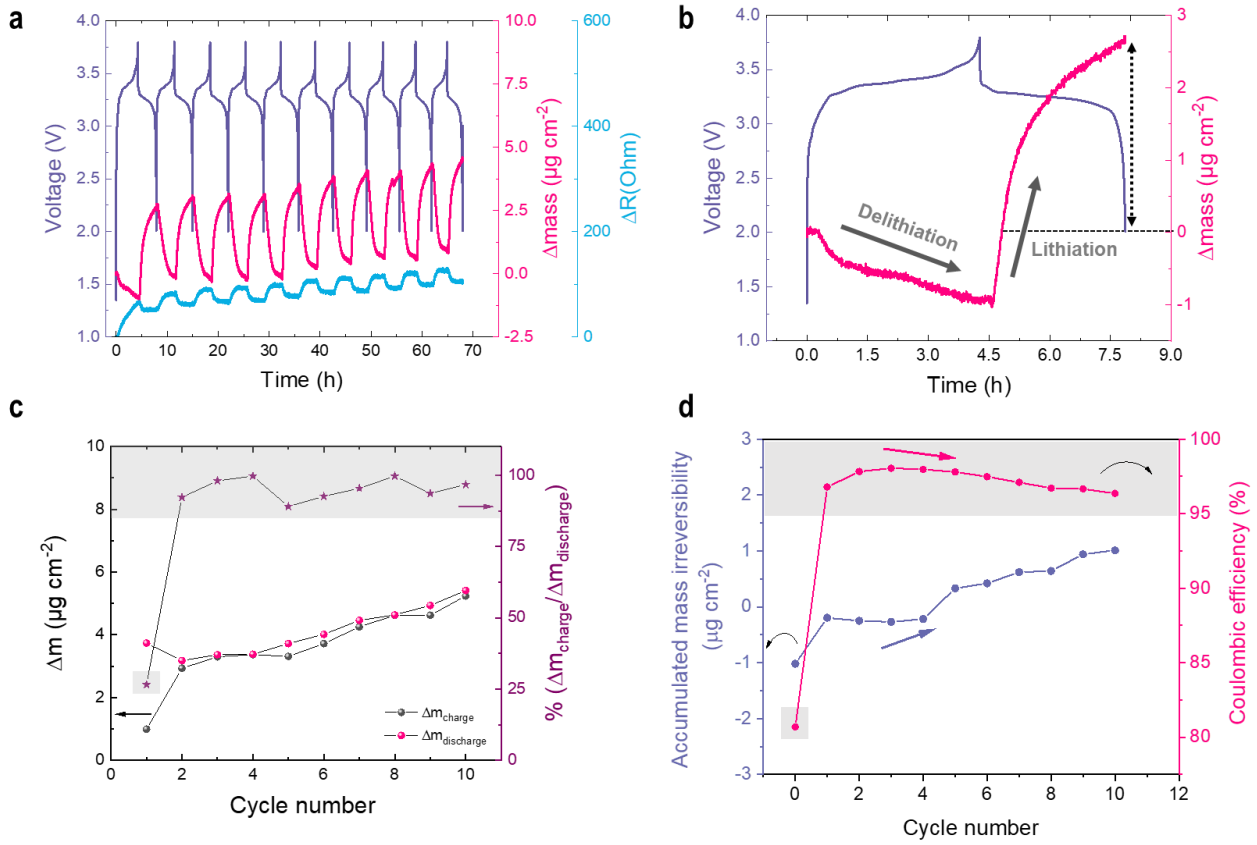

Figure 2. Charge/discharge profile of an LFP//Gr cell performed at a C/5 rate in LP30 electrolyte. **a)** the voltage, Δ*m* and Δ*R* as a function of cycling. WE-1 and WE-2 (shown in Fig. 1b) are the real working and loaded quartz resonator (LFP in this test), CE is the counter electrode (commercial Graphite electrode). The frequency change on LFP-coated QCM (~25 μg cm^{-2}) has been directly translated to mass change. **b)** first charge/discharge cycle, the mass irreversibility, believed to be related to the CEI formation, upon the end of the cycle is showcased with the dashed line and arrow. **c)** Δ*m* corresponding to charge and discharge of each cycle and their ratio $\Delta m_{charge}/\Delta m_{discharge}$ revealing the significant irreversibility in the first cycle. **d**) Accumulated irrevesible mass and coulombic efficiency variation throughout cycling.

Moreover, the magnitude of mass variation at the quartz electrode implies that a proportionate current is directed towards the smaller LFP electrode, consistent with Kirchhoff's law (**Figure 2a-2b**). Concomitantly, we observe a continuous increase in R_m (~70Ω) during the first charge after which it decreases by ~20Ω and becomes constant during the discharge process (**Figure 2a** and

S4a). This strongly indicates the formation of a viscoelastic layer corresponding to a cathodic interphase (CEI). An irreversibility in the overall mass exchange after the initial cycle (**Figure 2b**) further supports the presence of a cathodic interphase (CEI) formed on the cathode, despite the relatively moderate average potential of LFP (~3.45 V vs Li/Li^+) within the thermodynamically stable window of conventional Li-ion electrolytes. This phenomenon is predominantly attributed to the chemical degradation of electrolyte salt $LiPF_6$ in light of previous studies.[17b, 19]

Quantifying CEI is difficult in this case due to the simultaneous occurrence of two processes: lithium (de)insertion and electrolyte degradation (**Figure 2b**). Nonetheless, these findings can still provide insights into the CEI's quality, as subsequent cycles demonstrate relatively reversible mass response (an average $\Delta m_{charge}/\Delta m_{discharge}$ ratio above 90% is observed in **Figure 2c**) and a low amplitude in motional resistance change (< 20Ω) (**Figure S4b**). This indicates that the interphase formed may have effectively passivated the electrode surface. Note that the evolution of the frequency variation over time irreversibly drives the total curve upwards, most likely due to the exacerbation of the parasitic reaction arising from the higher electrolyte volume corroborated with a high floodness factor,[20] which is the ratio of the mass of the electrolyte and the mass of the active material which was found to be in our case ~100. This could result in thickening of the CEI on LFP. This is corroborated by the correlation between the decrease of the coulombic efficiency of our cell and the increase in accumulated irreversible mass calculated from the frequency drift (**Figure 2d**).

For the 4^{th} cycle, a total mass exchange of approximately 3 µg cm^{-2} is observed for the electrode loaded with 25 µg cm^{-2} of active material (**Figure 3a**) with a $\Delta m_{charge}/\Delta m_{discharge}$ ratio of ~1 (**Figure 2c**). Additionally, we observe the presence of two distinct slopes in the mass variation, indicating a potential difference in lithium insertion kinetics into the LFP cathode (**Figure 3a**). Moreover, if we assume the reversible value of 3 µg cm^{-2} to be exclusively corresponding to lithium insertion, the remaining 0.7 µg cm^{-2} in **Figure 2b** can be attributed to the mass of the formed CEI. Assuming that the interphase is predominantly LiF due to the chemical degradation of $LiPF_6$, we can calculate an approximate CEI thickness based on the density of LiF (2.64 g cm^{-3}) giving a thickness of 2.7 nm.

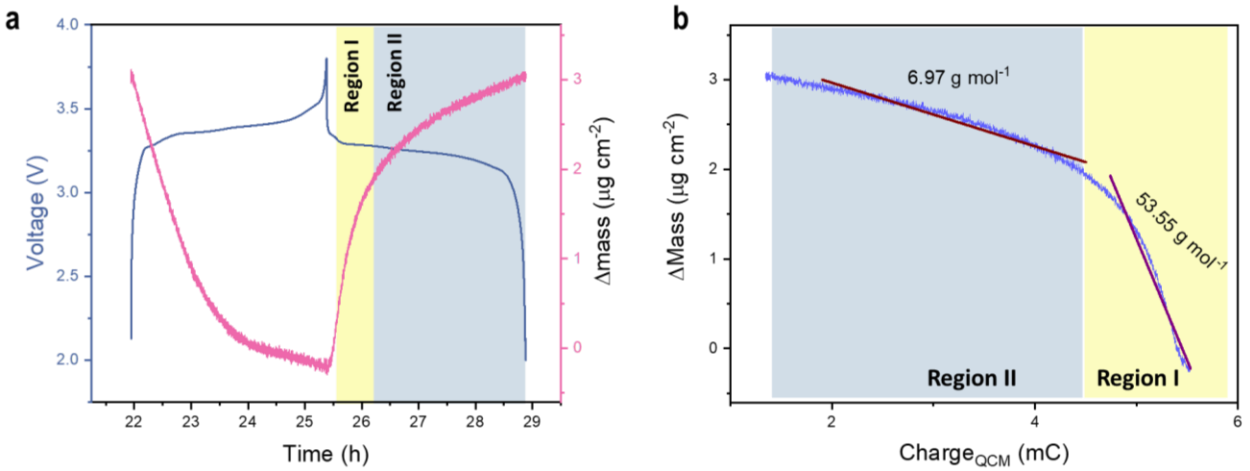

Figure 3. a) Voltage and mass variation profile during the 4th charge/discharge cycle of the LFP//Gr EQCM cell performed at a C/5 rate in LP30 electrolyte. The frequency change on LFP has been directly translated to mass change. **b)** Mass vs charge change of the discharge sequence of the 4th cycle. Both regions were fitted by linear regression and the apparent molar mass was estimated using Faraday's equation.

Next, we plot the Δm versus ΔQ curve (**Figure 3b**), from which we derive the average apparent molar mass (M_w) of the transferred species ($F\,\Delta m/\Delta Q = Mw/n$, with F is Faraday's number, Δm is mass change on the LFP-loaded QCM sensor, ΔQ charge variation, n is the number of electrons transferred). The amount of charge flowing into the sensor was estimated from the overall charge passing through both electrodes and using the QCM sensors' mass loading. The justification of this assumption and the conditions of its validity are given in the Supporting Information file, which describes a measurement of the currents passing through the two working electrodes separately.

During the discharge phase (lithiation), we observe two distinct kinetic regions and determine two different values for the mass per electron (M.P.E.). In region I, corresponding to the initial discharge stage, we calculate a value of approximately 53 g mol^{-1}. Subsequently, in region II the mass variation exhibits a slower rate, and we calculate a value of 6.97 g mol^{-1}, corresponding precisely to the insertion of Li-ions. It is plausible that at the onset of discharge, lithium is transferred in its solvated form due to the rapid deintercalation kinetics facilitated by the high state of charge (SOC) and fast diffusion coefficients of lithium into graphite.[21] The sharp variation of the motional resistance is an indicator of viscosity change at the vicinity of the electrode due to the mobility of the solvent molecules as observed in **Figure S5b (region I**). The more lithium is

extracted, the slower the diffusion kinetics become, leading to the second region where the desolvation process is no longer kinetically limited, and bare Li ions are transferred, consequently we observe no change in motional resistance due to the lower mobility of solvent molecules at the interface (**Figure S5b region II**). These findings contrast with the results obtained in half-cell EQCM measurements using cyclic voltammetry at 0.1 mV s^{-1} in 1M $LiClO_4$ in propylene carbonate, where solvent molecules were transferred close to the interface throughout the intercalation process and higher M.P.E. values were obtained.[5] This may highlight the impact of the negative electrode on the overall charge transfer mechanism. We could discuss this observation with the hypothesis that the introduction of graphite shows a rate-dependency of lithium insertion into LFP as the rate-limiting step appears to shift from desolvation to crystal diffusion during the charge/discharge sequences, as suggested by the different M.P.E values. It is recognized that further kinetic studies are necessary to prove this hypothesis, and other possible explanations such as the memory effect of LFP,[22] should be kept in mind. It is recalled that this intricacy cannot be detected in the former studies, since the EQCM measurements were done at half-cell configuration and GCD coupled QCM measurements at slower regime (C/5) failed due to its aforementioned limitations (**Figure 1c**).

3.1.2 $Na_3V_2(PO_4)_2F_3$ // Hard Carbon cell

Among the promising technologies for the commercialization of SIBs, the NVPF//HC system stands out due to its relatively high energy density of 120 Wh kg^{-1} (at cell level) but above all for its ability to deliver high power density of up to 5 kW kg^{-1}.[23] Additionally, this system offers cost-effectiveness, safety, and stable cycling performance over numerous charge-discharge cycles. However, challenges related to electrode-electrolyte interfaces can significantly impact system stability, with limited information available compared to Li-ion systems. Concerns include the second plateau of NVPF, positioned at 4.1V vs Na/Na^+ (~4.4V vs Li/Li^+), triggering severe electrolyte oxidation and rapid cell degradation. Furthermore, the high-potential operation leads to vanadium dissolution, contaminating the electrolyte and the negative electrode, ultimately causing cell failure. Thus, our desire is to gain deeper insights on interface processes, surpassing what has already been done on the same system in our earlier study using a half-cell EQCM configuration.[11]

The electrodes and the active material powder used here were obtained from Tiamat Energy (France).[24] The electrolyte used consists of 1M $NaPF_6$ in EC:PC:DMC. **Figure 4** displays the first charge/discharge cycle results of the NVPF//HC system with NVPF coated on the quartz and short-circuited to the composite NVPF electrode. The conformity of mass loss (gain) with the charge (discharge) processes confirms that the NVPF-loaded quartz follows the proper electrochemistry applied at the battery level (**Figure 4a** shows the discharge process).

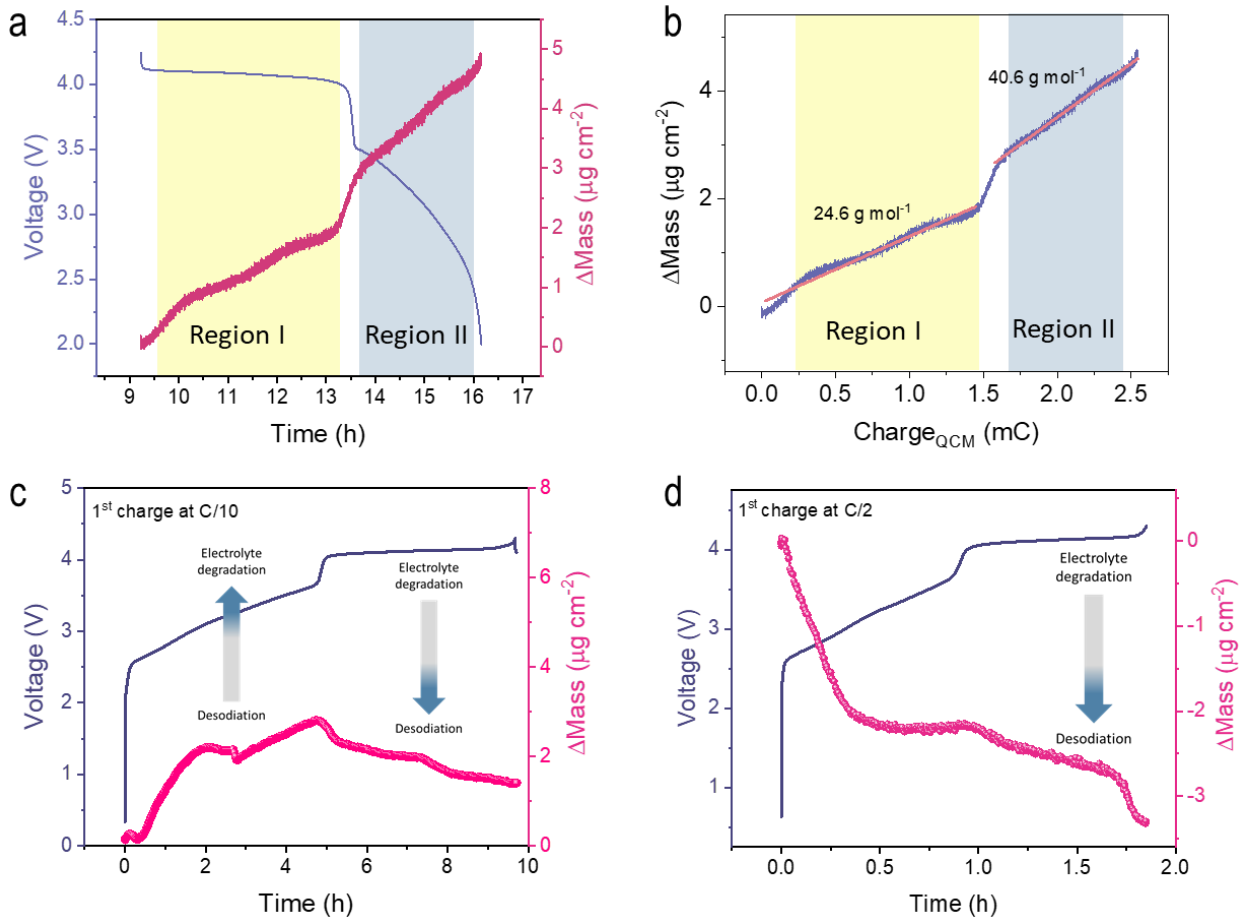

Figure 4. a) 1st discharge profile of NVPF//HC system where the NVPF-coated QCM sensor is short-circuited with the commercial NVPF cathode. The mass variation profile is superimposed. The experiment is performed at C/10 in 1M $NaPF_6$ in EC:PC:DMC, the corresponding M.P.E values are portrayed in **b)**. Voltage and mass variation profile of the NVPF coated resonator cycled at C/10 (**c**) and C/2 (**d**) (for both the 1st charge is shown). Arrows in **(c)** and **(d)** schematically show the competition between the electrolyte degradation and desodiation process.

The M.P.E. value calculated for the sodium insertion (discharge) show an agreement with bare sodium ion (~23 g mol^{-1}) and a second slope with a value of 41 g mol^{-1} which corresponds to solvated sodium or solvent molecules transferred to the electrode interface (**Figure 4b**). Similar to lithium insertion into LFP, two potential-related regions distinguishing both NVPF plateaus can be observed on the mass variation profile which further confirms the kinetic effect of the presence of an intercalation compound as an anode instead of alkali metal. Moreover, during the initial charge at C/10 (**Figure 4c**), the interplay between mass loss and gain resulting from simultaneous desodiation and electrolyte degradation processes becomes increasingly evident. Notably, we discern that the latter process predominantly influences the early stage of the charge process throughout NVPF's initial plateau at 3.7V vs Na/Na^+. To validate this observation, we conducted a three-electrode LSV experiment on our electrolyte (**Figure S7**), revealing oxidation peaks at approximately 3.5V and 4.1V. This substantiates that electrolyte oxidation primarily contributes to the observed mass intake early in the charging process.

The competition between mass loss and uptake is less apparent during the first charge at a faster rate (C/2). Here, the mass variation profile exhibits a predominantly negative trend due to the desodiation process, while electrolyte degradation is kinetically limited by the faster C-rate (**Figure 4d**). A similar pattern is observed in the motional resistance changes during these experiments (**Figure S8a-b**). Noticeably, ΔR_m increases in both cases, with a higher magnitude seen when cycling at a slower rate (~120 Ω at C/2 compared to ~180 Ω at C/10). However, the significant rise in ΔR_m at the C/2 rate indicates the presence of electrolyte degradation and formation of the CEI, despite continuous mass loss recorded during charge (**Figure 4d**). Upon discharge, a smaller variation in ΔR_m is noted (~6 Ω), suggesting the formation of a stable interphase at the C/10 rate (**Figure S8a**). However, during faster cycling, the amplitude of ΔR_m is greater (~20 Ω), pointing towards the formation of an unstable CEI (**Figure S8b**).

To further demonstrate the versatility of the cell design, we conducted an experiment where the active material coated onto the quartz was changed. This time, we sprayed HC on the quartz and short-circuited it to the actual HC electrode. HC exhibits a gradual profile that transitions into a quasi-plateau at lower potentials. **Figure 5a** displays the mass variation profile of the HC electrode, a relatively linear profile is observed throughout the sodiation process. Additionally, we observe a total mass irreversibility which may be due to parasitic reactions at lower potentials. Moreover, the calculated M.P.E. value (~21.7 g mol^{-1}) is close to that sodium ions throughout the intercalation

process (charge) (**Figure 5b**). Overall, this illustrate further the benefit of this new cell to evaluate electrode materials and interfaces in a more practical way.

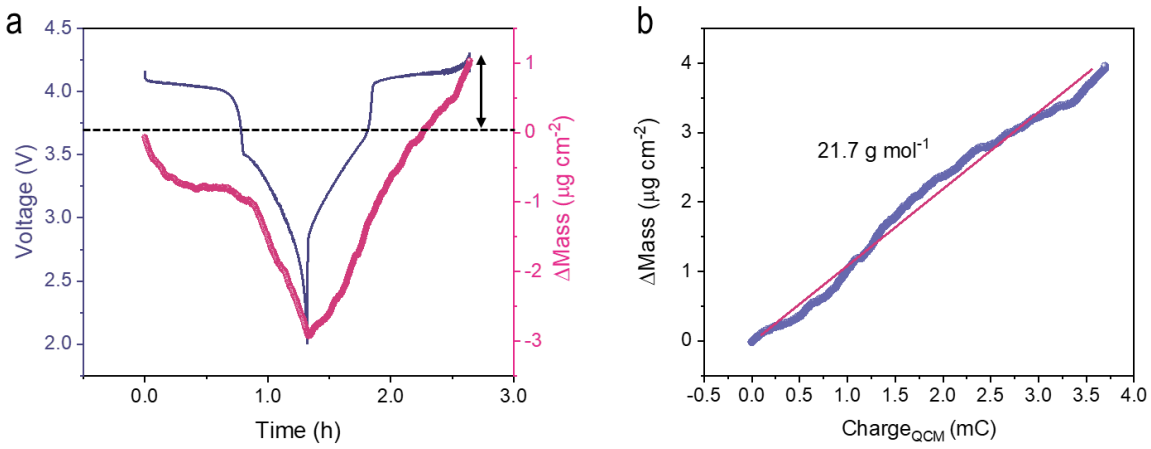

Figure 5. a) Voltage and mass variation profile at C/2 of the same system with the quartz coated with HC is short-circuited with the commercial HC anode and **b)** the corresponding M.P.E value on the charge process (sodium intercalation into HC) (the 5th cycle is shown here).

4. Conclusion

We have introduced a novel electrochemical apparatus designed to include a piezoelectric sensor for conducting precise microbalance frequency measurements during battery operation. This apparatus maintains a battery geometry that faithfully replicates real-world operational conditions, as experienced through the inspection of powder electrodes pertaining to two well-known Li-ion (LFP//Gr) and Na-ion (NVPF//HC) chemistries. Through the LFP//Gr study, we demonstrated notable differences in lithium insertion dynamics when using an intercalation compound as a counter-electrode instead of an alkali metal. We noted a change in the M.P.E value from approximately 53 g mol^{-1} to ~7 g mol^{-1}, corresponding to a change in the rate-limiting step in the charge transfer process. Initially, desolvation of lithium ions was evidently the hindering step, but as the process progressed, diffusion in either the interphase or the crystal structure became the rate-limiting factor. This behavior was not observed in the half-cell experiment using lithium as the negative electrode.

The versatility of the new cell design was further shown on the NVPF//HC chemistry. By short-circuiting the QCM electrode with the cell's cathode or anode electrodes, the QCM electrode effectively acted as an extension of the cathode or anode electrode under test. On the basis of this set-up, we could estimate two different species, namely bare and solvated sodium ions, participating to the interface process at higher and lower potentials, respectively. It was also possible to do the same type of test, this time by short-circuiting the anode side with a hard carbon coated QCM sensor, and here we observed a net mass gain even after several cycles. Moreover, we provide evidences during discharge of a competition between the desodiation and degradation processes, leading to a net mass gain probably related to the SEI formation. Overall these results highlight the great potential of this new cell design for interrogating plausible interactions, ion intercalation, interphase formation, cross-talk *etc.*, in various cell chemistries.

However, several improvements to the present work are immediately apparent and range from shortening the distance between the QCM sensor and the real cathode or anode electrode to using a co-planar configuration where both working electrodes would be at the same level, for enhancing signal quality at higher cycling rates to exploring other chemistries beyond Li(Na)-ion. Reducing the distance between the counter electrode and the QCM sensor can also suppress the larger inherent ohmic drop at the quartz level observed in the current measurement experiment (**Figure S6**). Having demonstrated the concept of EQCM coupled with GCD experiments, we are also considering engineering improvements aimed at limiting the volume footprint and reducing the weight of the current design. In addition, more prospectively, efforts are underway to modify the current cell to perform simultaneously EQCM and IR measurements so as to obtain insights into chemical composition of the SEI and CEI. We hope that the strategy described here, which focuses on operando evaluation of the interface under practical conditions, will lead to a better understanding of how to mitigate interfacial problems in battery chemistry and will challenge the preconceived notion that EQCM is limited solely to pure fundamental research.

Associated Content

State-of-the-art on the EQCM cell designs and limitations, new cell design details and schemes, and additional data on the LFP//Gr and NVPF//HC cells monitored by QCM sensors.

Conflict of Interest

The authors declare the filing of a European patent concerning the cell design described in this paper.

Acknowledgements

EB, OS and JMT acknowledge the "Sorbonne Université - Programme doctoral Génie des Procédés" for the PhD scholarship. OS and JMT also acknowledge the funding from DIM-RESPORE.

Table of Contents (TOC)

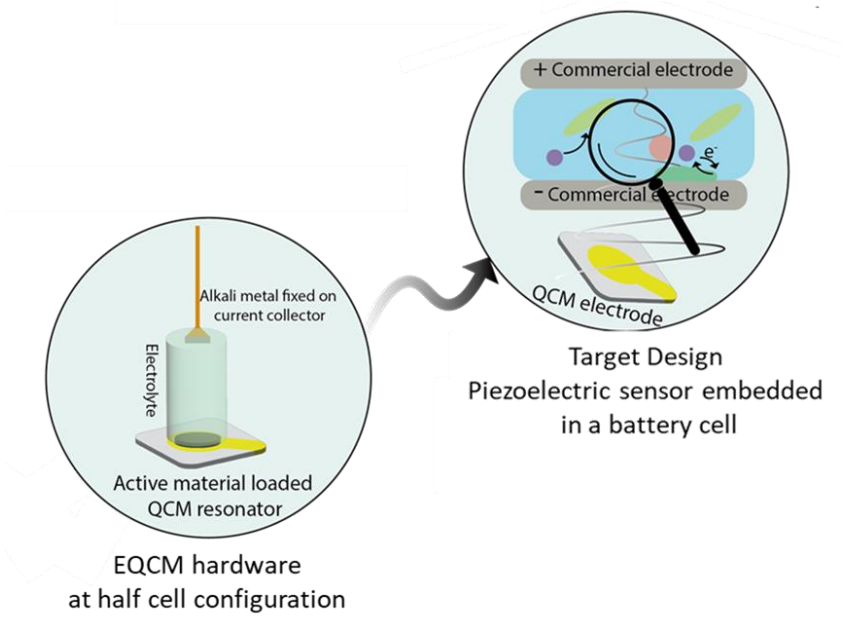

A novel battery cell design was introduced which integrates piezoelectric sensors for surface-sensitive operando measurements. This enables operando electrogravimetry to be realized, and the electrochemistry of a battery to be more faithfully reproduced at the sensor level. Proof of concept

on both Li-ion and Na-ion systems highlights the great potential of the cell for interrogating ion intercalation, interphase-formation, cross-talk *etc*.

References

[1] J. Liu, J. Xiao, J. Yang, W. Wang, Y. Shao, P. Liu, M. S. Whittingham, *Next Energy* **2023**, 1, 100015.

[2] J. Huang, S. T. Boles, J.-M. Tarascon, *Nat. Sustain.* **2022**, 5, 194.

[3] S. Schweidler, M. Bianchini, P. Hartmann, T. Brezesinski, J. Janek, *Batteries & Supercaps* **2020**, 3, 1021.

[4] A. R. Hillman, *J. Solid State Electrochem.* **2011**, 15, 1647.

[5] P. Lemaire, T. Dargon, D. Alves Dalla Corte, O. Sel, H. Perrot, J.-M. Tarascon, *Anal. Chem.* **2020**, 92, 13803.

[6] a) N. Shpigel, M. D. Levi, D. Aurbach, *Energy Storage Mater.* **2019**, 21, 399; b) P. G. Kitz, P. Novák, E. J. Berg, *ACS Appl. Mater. Interfaces* **2020**, 12, 15934.

[7] a) C. R. Arias, C. Debiemme-Chouvy, C. Gabrielli, C. Laberty-Robert, A. Pailleret, H. Perrot, O. Sel, *J. Phys. Chem. C* **2014**, 118, 26551; b) E. Bendadesse, A. V. Morozov, A. M. Abakumov, H. Perrot, J.-M. Tarascon, O. Sel, *ACS Nano* **2022**, 16, 14907.

[8] P. G. Kitz, M. J. Lacey, P. Novák, E. J. Berg, *Anal. Chem.* **2019**, 91, 2296.

[9] a) N. Shpigel, M. D. Levi, S. Sigalov, L. Daikhin, D. Aurbach, *Acc. Chem. Res.* **2018**, 51, 69; b) N. Shpigel, S. Sigalov, M. D. Levi, T. Mathis, L. Daikhin, A. Janes, E. Lust, Y. Gogotsi, D. Aurbach, *Joule* **2018**, 2, 988.

[10] N. Mozhzhukhina, E. Flores, R. Lundström, V. Nyström, P. G. Kitz, K. Edström, E. J. Berg, *J. Phys. Chem. Lett.* **2020**, 11, 4119.

[11] E. Bendadesse, C. Gervillié-Mouravieff, C. Leau, K. Goloviznina, F. Rabuel, M. Salanne, J.-M. Tarascon, O. Sel, *Adv. Energy Mater.* **2023**, 13, 2300930.

[12] P. Lemaire, A. Serva, M. Salanne, G. Rousse, H. Perrot, O. Sel, J.-M. Tarascon, *ACS Appl. Mater. Interfaces* **2022**, 14, 20835.

[13] Z. Yang, A. A. Gewirth, L. Trahey, *ACS Appl. Mater. Interfaces* **2015**, 7, 6557.

[14] J. Kasnatscheew, T. Placke, B. Streipert, S. Rothermel, R. Wagner, P. Meister, I. C. Laskovic, M. Winter, *J. Electrochem. Soc.* **2017**, 164, A2479.

[15] G. Sauerbrey, *Z. Phys. B: Condens. Matter* **1959**, 155, 206.

[16] L. L. D. Alves Dalla Corte, P. Lemaire, T. Dargon *Patent EP3757062A1*, **2020**.

[17] a) M. Woody, M. Arbabzadeh, G. M. Lewis, G. A. Keoleian, A. Stefanopoulou, *J. Energy Storage* **2020**, 28, 101231; b) M. Safari, C. Delacourt, *J. Electrochem. Soc.* **2011**, 158, A1123; c) M. Simolka, J. F. Heger, H. Kaess, I. Biswas, K. A. Friedrich, *J. Appl. Electrochem.* **2020**, 50, 1101.

[18] a) M. Koltypin, D. Aurbach, L. Nazar, B. Ellis, *Electrochem. Solid-State Lett.* **2007**, 10, A40; b) H. Zheng, L. Tan, L. Zhang, Q. Qu, Z. Wan, Y. Wang, M. Shen, H. Zheng, *Electrochim. Acta* **2015**, 173, 323.

[19] E. W. C. Spotte-Smith, T. B. Petrocelli, H. D. Patel, S. M. Blau, K. A. Persson, *ACS Energy Letters* **2023**, 8, 347.

[20] V. Dargel, N. Shpigel, S. Sigalov, P. Nayak, M. D. Levi, L. Daikhin, D. Aurbach, *Nature Communications* **2017**, 8, 1389.

[21] a) H. Yang, H. J. Bang, J. Prakash, *J. Electrochem. Soc.* **2004**, 151, A1247; b) H. Zhang, Y. Yang, D. Ren, L. Wang, X. He, *Energy Storage Mater.* **2021**, 36, 147.

[22] T. Sasaki, Y. Ukyo, P. Novák, *Nat. Mater.* **2013**, 12, 569.
[23] a) J.-M. Tarascon, *Joule* **2020**, 4, 1616; b) I. Hasa, S. Mariyappan, D. Saurel, P. Adelhelm, A. Y. Koposov, C. Masquelier, L. Croguennec, M. Casas-Cabanas, *J. Power Sources* **2021**, 482, 228872.
[24] http://www.tiamat-energy.com.